

Quality-controlled meteorological datasets from SIGMA automatic weather stations in northwest Greenland, 2012–2020

Motoshi Nishimura^{1*}, Teruo Aoki¹, Masashi Niwano², Sumito Matoba³, Tomonori Tanikawa², Tetsuhide Yamasaki⁴, Satoru Yamaguchi⁵, Koji Fujita⁶

¹National Institute of Polar Research, Tokyo, Japan

²Meteorological Research Institute, Japan Meteorological Agency, Ibaraki, Japan

³Institute of Low Temperature Science, Hokkaido University, Hokkaido, Japan

⁴Avangnaq Arctic Project, Osaka, Japan

⁵Snow and Ice Research Center, National Research Institute for Earth Science and Disaster Resilience, Niigata, Japan

⁶Graduate School of Environmental Studies, Nagoya University, Nagoya, Japan

Correspondence to: Motoshi Nishimura (nishimura.motoshi@nipr.ac.jp)

Abstract. In situ meteorological data are essential to better understand ongoing environmental changes in the Arctic. Here, we present a dataset of quality-controlled meteorological observations by two automatic weather stations in northwest Greenland from July 2012 to the end of August 2020. The stations were installed in the accumulation area on the Greenland Ice Sheet (SIGMA-A site, 1490 m a.s.l.) and near the equilibrium line of the Qaanaaq Ice Cap (SIGMA-B site, 944 m a.s.l.). We describe the two-step sequence of quality-control procedures that we used to create increasingly reliable datasets by masking erroneous data records. Those data sets are archived in the Arctic Data archive System (ADS) (SIGMA-A; <http://doi.org/10.17592/001.2022041303>, SIGMA-B; <http://doi.org/10.17592/001.2022041306>). We analyzed the resulting 2012–2020 time series of air temperature, surface height, surface albedo, and histograms of longwave radiation (a proxy of cloudiness). We found that surface height increased and no significant albedo decline in summer was observed at the SIGMA-A site. In contrast, high air temperatures and frequent clear-sky conditions in the summers of 2015, 2019, and 2020 at the SIGMA-B site caused significant albedo and surface lowering. Therefore, it appears that these weather condition difference, and it led to apparent surface height decrease at the SIGMA-B site but not at the SIGMA-A site. We anticipate that this quality-control method and these datasets will aid in climate studies of northwest Greenland as well as contribute to the advancement of broader polar climate studies.

31 1. Introduction

32 Automatic weather observation in Greenland started with GC-Net (Greenland Climate Network;
33 Steffen and Box, 2001), which was established as a network of automatic weather stations (AWS) in
34 Greenland after 1990. This observation network intended to provide long-term observations of
35 climatological and glaciological factors over Greenland. This was followed by the PROMICE (van As
36 et al., 2011; Fausto et al., 2021) led by the Geological Survey of Denmark and Greenland (GEUS) and
37 the K-transect network (van de Wal et al., 2005), led by Utrecht University in the Netherlands, has
38 been deployed. PROMICE is currently operating the largest observation network in Greenland by
39 contracting the maintenance of GC-Net equipment, and K-transect has deployed equipment mainly in
40 the western part of the country and continues to monitor the area closely. Both networks have provided
41 important long-term meteorological data.

42 To contribute to these efforts and to fill a spatial gap, we established two AWS systems in northwest
43 Greenland (Fig. 1), where rapid environmental changes have occurred in recent years (Aoki et al.,
44 2014). Recent studies of this region have documented a drastic mass loss since the mid-2000s
45 (Mouginot et al., 2019), an expansion of the ablation area (Noël et al., 2019), and a hot spot of
46 increasing rainfall (Niwano et al., 2021). The two sites were established in 2012 as a part of the Snow
47 Impurity and Glacial Microbe effects on abrupt warming in the Arctic (SIGMA) Project, which aimed
48 to clarify the dramatic enhancement of melting of the Greenland Ice Sheet induced by snow impurities
49 (e.g., black carbon, mineral dust). The observational data acquired since that time have been used by
50 glaciological (Yamaguchi et al., 2014; Tsutaki et al., 2017; Matoba et al., 2018; Kurosaki et al., 2020),
51 meteorological (Aoki et al., 2014; Tanikawa et al., 2014; Niwano et al., 2015; Hirose et al., 2021), and
52 biological studies (Onuma et al., 2018; Takeuchi et al., 2018). These data are also valuable because
53 they support the evaluation and development of numerical models (e.g., Niwano et al., 2018; Fujita et
54 al., 2021).

55 The datasets from AWS generally contain erroneous data records that are attributed to natural
56 factors (e.g., riming, ice accretion, snow accumulation on sensors) or technical issues (e.g., Zero
57 Offset; Behrens, 2021, faulty sensors) for radiation sensors. Various procedures exist for improving
58 the quality of such datasets (e.g., Fiebrich et al., 2010; Fausto et al., 2021). In particular, careful Quality
59 Control (QC) procedures, which is a process to improve the quality of data by removing outliers, are
60 required for downward radiation sensors, which are sensitive to solar zenith angle, icing, riming, and
61 snowfall (van den Broeke et al., 2004a, b; Moradi, 2009). Other QC procedures deal with error sources
62 through range, step, and internal consistency tests (Estévez et al., 2011). The specifics of QC methods,
63 for example, the threshold value for detecting erroneous data records, should be adjusted for each
64 observation environment. In this paper, we describe the QC methods used for the in situ meteorological
65 observation data from northwest Greenland, which include existing QC methods, new ones, and
66 combinations of both.

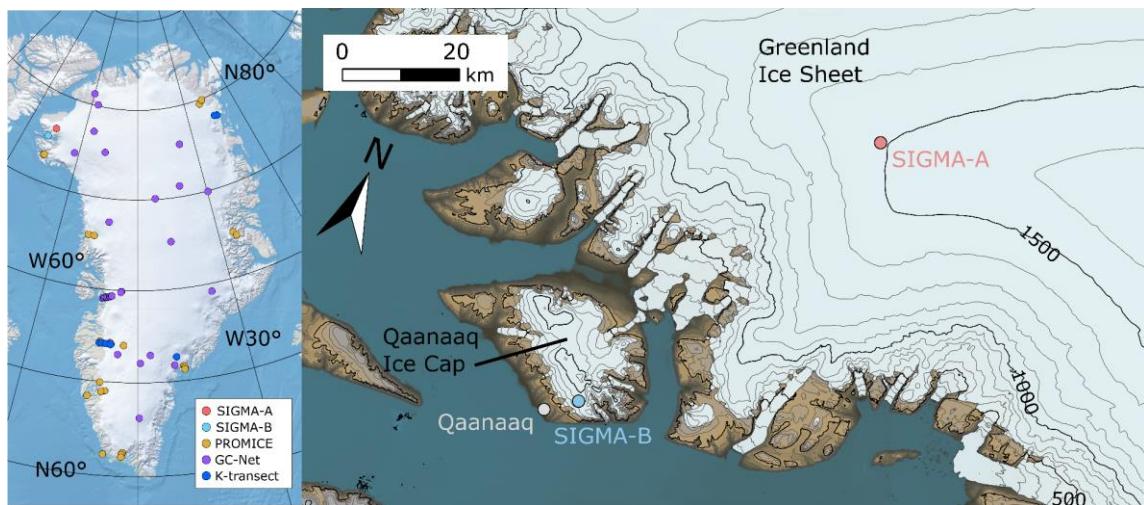
67 After describing the AWS sites (Sect. 2) and their datasets (Sect. 3), this paper introduces the two
68 separate QC methods used sequentially to mask erroneous data records (Sect. 4). We then present
69 examples of time series of meteorological variables in northwest Greenland, infer their implications
70 for interannual variations in weather conditions, and describe the differences between the two sites
71 (Sect. 5).

72 2. AWS general description

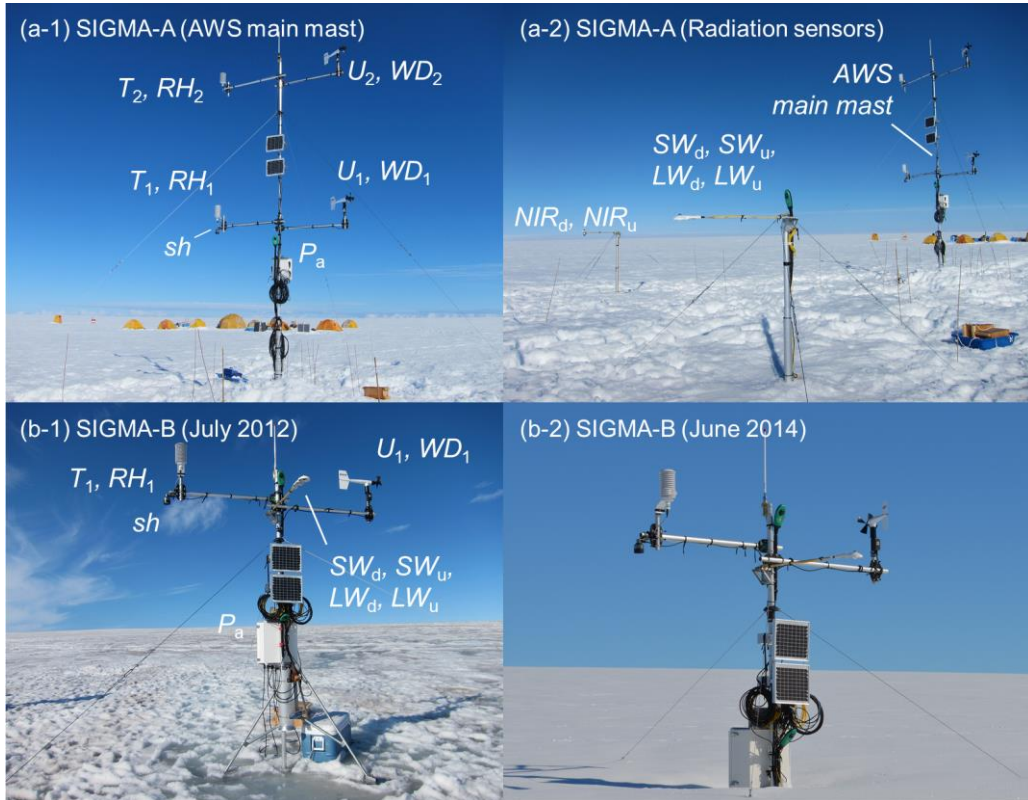
73 The two AWSs are installed at the SIGMA-A site (78.052° N, 67.628° W; 1490 m a.s.l.), on the
74 northwest Greenland Ice Sheet, and the SIGMA-B site (77.518° N, 69.062° W; 944 m a.s.l.), on the
75 Qaanaaq Ice Cap, a peripheral ice cap on the Greenland coast (Fig. 1). They have been in operation
76 since July 2012 (Aoki et al., 2014). The observed parameters and the sensor specifications including
77 abbreviations are listed in Table 1. The other key constants, variables, and their abbreviations used in
78 this study are also in Table 2.

79 The SIGMA-A site is 70 km inland from the coast on a ridge of the Greenland Ice Sheet extending
80 northwest from the Greenland Summit; it sits on a flat snow surface with no obstacles around the site
81 (see Fig. 2). This site is in an accumulation area of the ice sheet (Matoba et al., 2018) based on the
82 analysis of ice-core data (Yamaguchi et al., 2014; Matoba et al., 2017). The SIGMA-B site is 3 km
83 north of the village of Qaanaaq. This site is considered to be located near the equilibrium line (910 m
84 a.s.l.; Tsutaki et al., 2017) on the Qaanaaq Ice Cap, which ranges in elevation between 30 and 1110 m
85 a.s.l. (Sugiyama et al., 2014). The surface condition at this site varies (see Fig. 2), and significant
86 surface lowering has occurred in warm years (e.g., Aoki et al., 2014). The site is located on a
87 southwest-facing slope (azimuth 220°) with an angle of 4° according to 10 m DEM data (Porter et al.,
88 2018).

89



91 Figure 1. Location map of Greenland showing PROMICE, GC-Net, and K-transect AWS sites (left)
 92 and a local map of northwest Greenland showing locations of AWS sites SIGMA-A and SIGMA-B.
 93 Contour interval in the right panel is 100 m.
 94



95
 96 Figure 2. Setting and instrumentation at the SIGMA-A site (top) and the SIGMA-B site (bottom).
 97 Surface conditions at SIGMA-B are shown in July 2012 and June 2014. Sensors are labeled with the
 98 observation parameters they measure (see Table 1).
 99

100 Table 1. Meteorological observation parameters and sensor specifications.

observation parameter	abbreviation	unit	sensor	observation range	accuracy
wind speed	U_n^a	m s^{-1}	Young, 05103	0 to 100 [m s^{-1}]	$\pm 0.3 \text{ m s}^{-1}$ or 1%
wind direction	WD_n^a	degree	Young, 05103	360° mechanical, 355° electrical (5° open)	$\pm 3^\circ$
air temperature	T_n^a	$^\circ\text{C}$	Vaisala, HMP155 ^b	-80 to +60 [$^\circ\text{C}$]	$\pm 0.17 \text{ }^\circ\text{C}$
relative humidity ^c	RH_n^a	%	Vaisala, HMP155 ^b	0 to 100%	$\pm 1\%$ (0 to 90%) $\pm 1.7\%$ (90 to 100%)
atmospheric pressure	P_a	hPa	Vaisala, PTB210	500 to 1100 [hPa]	$\pm 0.30 \text{ hPa}$ at 20 $^\circ\text{C}$
downward and upward shortwave radiation	SW_d, SW_u	W m^{-2}	Kipp & Zonen, CNR4	0.3 to 2.8 [μm]	$\pm 5\%$ (daily total)
downward and upward longwave radiation	LW_d, LW_u	W m^{-2}	Kipp & Zonen, CNR4	4.5 to 42 [μm]	$\pm 10\%$ (daily total)
downward and upward near-infrared radiation	NIR_d, NIR_u	W m^{-2}	Kipp & Zonen, CMP6 with a RG715 cut-off filter	0.715 to 2.8 [μm]	$\pm 5\%$ (daily total)
surface height	sh	cm	Campbell, SR50	0.5 to 10 [m]	1 cm or 0.4%
snow temperature	st_n^a	$^\circ\text{C}$	Climatic, C-PTWP-10	-40 to +60 [$^\circ\text{C}$]	$\pm 0.15 \text{ }^\circ\text{C}$
tilts of the main mast	$Tilt_x, Tilt_y$	degree	TURCK, B2N85H-Q20L60-	-85° to +85°	$\pm 0.5^\circ$

a: "n" suffix is appended to distinguish the observation height or depth.
 b: protected from direct solar irradiance by a naturally-aspirated 14-plate Gill radiation shield
 c: Relative humidity is measured relative to water even in sub-freezing environments

symbol	name	value	unit
constant			
f_{nir}	a fraction of near-infrared radiant flux in the shortwave radiant flux at the top of the atmosphere	0.5151	no dimension
I_0	solar constant	1361	$W m^{-2}$
n	cloud cover coefficient	0.5	no dimension
r_m	annual mean distance between the Sun and the Earth	1.496×10^8	km
$sh_{initial}$	initial height of the surface height sensor	300	cm
$\alpha_{sw,max}$	maximum value of surface albedo	0.95	no dimension
$\alpha_{nir,max}$	maximum value of surface near-infrared albedo	0.90	no dimension
K	constant depending on cloud type	0.26	no dimension
ε	snow/ice surface emissivity	0.98	no dimension
σ	Stefan-Boltzmann constant	5.67×10^8	$W m^{-2} K^{-4}$
variable			
d	diffuse fraction in global radiation		no dimension
I_d	diffuse solar radiation		$W m^{-2}$
I_s	direct solar radiation		$W m^{-2}$
LW_d	downward longwave radiation		$W m^{-2}$
LW_{std}	standard atmospheric longwave radiation		$W m^{-2}$
LW_u	upward longwave radiation		$W m^{-2}$
NIR_d	downward near-infrared radiation		$W m^{-2}$
NIR_u	upward near-infrared radiation		$W m^{-2}$
P_a	atmospheric pressure		hPa
r	distance between the Sun and the Earth		m
$RH_{1,2}^a$	relative humidity		%
sh	surface height		cm
sh_{raw}	raw data of surface height		m
$solz$	solar zenith angle		degree
$solz_{slope}$	solar zenith angle for a slope		degree
st_{1-6}^b	snow temperature		$^{\circ}C$
$st_{depth}_{1-6}^b$	snow temperature sensor depth		cm
SW_d	downward shortwave radiation		$W m^{-2}$
$SW_{d,slope}$	downward shortwave radiation for a slope		$W m^{-2}$
SW_{TOA}	downward shortwave radiation at the top of the atmosphere		$W m^{-2}$
SW_u	upward shortwave radiation		$W m^{-2}$
t_r	transmissivity of the atmosphere for shortwave radiation		no dimension
$T_{1,2}^a$	air temperature		$^{\circ}C$
$WD_{1,2}^a$	wind direction		degree
$U_{1,2}^a$	wind speed		$m s^{-1}$
α_{sw}	surface albedo		no dimension
$\alpha_{sw,i}$	daily integrated surface albedo		no dimension
α_{nir}	surface near-infrared albedo		no dimension
$\alpha_{nir,i}$	daily integrated surface near-infrared albedo		no dimension
β	slope angle		radian
ε_0	clear-sky atmospheric emissivity		no dimension
ε^*	atmospheric emissivity		no dimension
θ	solar zenith angle		radian
θ_{slope}	solar zenith angle for a slope		radian
ϕ	solar azimuth angle		radian
ϕ_{slope}	solar azimuth angle of a slope		radian

^a 1: observed at lower height, 2: observed at upper height (only at the SIGMA-A site)

^b 1-6: observing depth

105

106 3. Description of AWS systems and datasets

107 3.1. Specifications

108 Each AWS main mast is set in a hole drilled using a hand auger. Sensors for air temperature,
109 relative humidity, and wind speed and direction are mounted at the ends of horizontal poles to exclude
110 possible thermal and wind disturbances from the main mast. The SIGMA-A sensors are placed 3 m
111 and 6 m above the surface, as signified by subscripts “1” (lower) and “2” (upper) in the corresponding
112 data variables. The SIGMA-B sensors are set at 3 m above the surface and have subscripts of “1”. The
113 surface height sensor at both sites is mounted at 3 m height beneath the air temperature and relative
114 humidity sensors. Six snow temperature sensors have been set as follows. Four sensors were set at
115 19:00 UTC on 29 June 2012 at depths of 100 cm (st_1), 70 cm (st_2), 40 cm (st_3), and 5 cm (st_4) below
116 the snow surface. At 21:00 UTC on 27 July 2013, sensors st_3 and st_4 were relocated to depths of 46
117 cm and 16 cm, respectively. Sensors st_5 and st_6 were set at 5 cm under the surface and 45 cm above
118 the surface, respectively, at 14:00 UTC on 9 June 2014. Sensors for shortwave, longwave, and near-
119 infrared radiation are installed at SIGMA-A on separate poles 10 m from the main mast (Fig. 2a-2). A
120 pyranometer and a pyrgeometer at SIGMA-B are mounted on the main mast facing directly south. Tilt
121 angles of the main mast in the north-south ($Tilt_x$) and east-west ($Tilt_y$) directions are monitored with
122 an inclinometer attached to the main mast. The additional suffix “A” or “B” represents the site name
123 in the variables introduced below.

124 Electric power is supplied to the AWS systems by a lead-acid battery that is charged constantly by
125 solar panels attached to the main mast. All parameters are recorded once per minute and stored in a
126 data logger (C-CR1000, Campbell Scientific, USA), except for the main mast’s surface height and tilt
127 angles, which are recorded every hour. Hourly data are calculated for the other parameters by
128 averaging the 1-min data. All hourly data are sent regularly to the data server via the Argos satellite
129 channel.

130 Surface height is measured with an ultrasonic snow gauge (Table 1). The raw data from this sensor
131 (sh_{raw}) is the distance from the sensor to the snow surface, which has a temperature dependence. The
132 temperature-corrected surface height (sh) is calculated from

$$133 \quad sh = sh_{initial} - sh_{raw} \times \sqrt{\frac{T_2 + 273.15}{273.15}} \times 100, \quad (i)$$

134 where $sh_{initial}$ (= 300 cm) is the initially installed sensor height from the surface and T_2 is air
135 temperature.

136

137 3.2. Data processing

138 We describe the calculations for some variables used in the QC process in this section. To
 139 accurately calculate the surface albedo and surface energy balance at the SIGMA-B site, we considered
 140 the impact of the sloping surface on the vertical radiant flux. To account for this effect, we derived the
 141 slope-corrected downward shortwave radiation (SW_{d_slope}) using the methods in Jonsell et al. (2003)
 142 and Hock and Holmgren (2005). The SW_{d_slope} is calculated by

$$143 \quad SW_{d_slope} = I_s + I_d, \quad (ii)$$

144 where I_s and I_d are the direct and diffuse shortwave radiation for a slope, respectively:

$$145 \quad I_s = SW_d \times d, \quad (iii)$$

$$146 \quad I_d = SW_d \times (1 - d) \times \frac{\cos \theta_{slope}}{\cos \theta}, \quad (iv)$$

147 where d is the ratio of total diffuse radiation to global radiation and θ and θ_{slope} [radian] are the solar
 148 zenith angle and the solar zenith angle for a slope, respectively. The ratio d is obtained from
 149 atmospheric transmittance t_r by

$$150 \quad d = \begin{cases} 0.15 & \text{for } 0.8 \leq t_r, \\ 0.929 + 1.134t_r - 5.111t_r^2 + 3.106t_r^3 & \text{for } 0.15 < t_r < 0.8, \\ 1.0 & \text{for } t_r \leq 0.15, \end{cases} \quad (v)$$

151 where

$$152 \quad t_r = \frac{SW_d}{SW_{TOA}}, \quad (vi)$$

153 where SW_{TOA} is the downward shortwave radiation at the top of the atmosphere, calculated by

$$154 \quad SW_{TOA} = I_0 \left(\frac{r_m}{r} \right)^2 \cos \theta, \quad (vii)$$

155 where I_0 ($= 1361 \text{ W m}^{-2}$) is the solar constant (Rottman, 2006; Fröhlich, 2012), r is the distance
 156 between the Sun and the Earth (assuming an elliptical orbit with an eccentricity of 0.01637), and r_m is
 157 its annual mean ($= 1.496 \times 10^8 \text{ km}$).

158 The solar zenith angle for a slope in Eq. (iv) is calculated by

$$159 \quad \cos \theta_{slope} = \cos \beta \cos \theta + \sin \beta \sin \theta \cos(\varphi - \varphi_{slope}), \quad (viii)$$

160 where β is the slope angle from a horizontal plane, and φ and φ_{slope} are the solar azimuth and the solar
 161 azimuth for the slope direction, respectively. Solar zenith and azimuth angles are calculated from the
 162 geographic position of the observation site and the date and time.

163 Shortwave and near-infrared albedos (a_{sw} and a_{nir} , respectively) are calculated as the ratio of
 164 upward and downward radiant fluxes, as shown for a_{sw} by

$$165 \quad \alpha_{sw} = \frac{SW_u}{SW_d}, \quad (ix)$$

166 where SW_u is the upward shortwave radiant flux and SW_d is the downward shortwave radiant flux.

167 SW_{d_slope} is used for SW_d when calculating a_{sw} at the SIGMA-B site. The daily integrated shortwave
168 albedo ($a_{sw,i}$) is calculated as the ratio of cumulative upward and downward radiant fluxes for the past
169 24 h:

$$170 \quad \alpha_{sw,i} = \sum_{24h} SW_u / \sum_{24h} SW_d. \quad (x)$$

171 The near-infrared albedo (a_{nir}) and daily integrated near-infrared albedo ($a_{nir,i}$) are calculated in the
172 same way. The near-infrared fraction is the ratio of the downward near-infrared radiant flux (NIR_d) to
173 SW_d .

174 Note that some parameters may require correction or caution depending on the observation
175 environment. First, since temperature and humidity shelters are naturally ventilated, air temperature
176 value may have a positive bias due to shelter heating from solar radiation (e.g., Morino et al, 2021).
177 In addition, in sub-freezing conditions, relative humidity may not be measured correctly because the
178 sensor used in this study (Vaisala, HMP155) calculates relative humidity as liquid water vapor pressure
179 even in sub-freezing environments and when the shelter is covered by rime or frost (Makkonen and
180 Laakso, 2005). Aoki et al. (2011) pointed out that the pole on which the radiometer is mounted casts
181 a shadow on the radiation sensor. In addition, reflected and shielding scattered radiations due to the
182 AWS including solar panels may result in incorrect radiation measurements, although no anomalous
183 radiation data due to these factors were found. Although the possibility of data correction as described
184 above is recognized, the focus of this paper is to open the observed values themselves, without any
185 correction or data processing that might involve the implementer's intention. Therefore, we will note
186 only the correction possibilities and present the observed data in this study.

187 **4. Quality control**

188 The datasets of observations at sites SIGMA-A and SIGMA-B are classified into four QC levels
189 numbered 1.0 to 1.3. A Level 1.0 dataset, which is not archived in any repository, is a raw dataset
190 without data processing. A Level 1.1 dataset is a raw dataset with flags added to indicate missing data
191 for periods when the data logger was inoperative. A Level 1.2 dataset has undergone an initial control,
192 which uses a simple masking algorithm to eliminate anomalous values that violate physical laws or
193 are impossible in the observed environment. The initial control improves the accuracy of the statistical
194 processing that follows and reduces the possibility of excluding true values. A Level 1.3 dataset has
195 undergone a secondary control, in which statistical methods are used on Level 1.2 data to identify and
196 mask outlier values. It has also undergone a final manual masking procedure, in which a researcher
197 visually checks the dataset and masks outliers based on subjective criteria.

198 The initial control method is described in Sect. 4.1 and the secondary control method is described
199 in Sect. 4.2. In these sections, the parameter suffixes related to the differences in observation height
200 (1 and 2) and sites (A and B) are omitted except when needed for clarity, and subscripts indicating

201 upward and downward radiation (d; downward, u; upward) is denoted as χ in the equation. Erroneous
202 records are flagged with one of the following numerical expressions to signify the reason they have
203 been flagged:

204 –9999: a missing or erroneous data record attributed to a mechanical malfunction or a local
205 phenomenon such as sensor icing, riming, or burial in snow.

206 –9998: an erroneous radiation record when the radiant sensor was covered with snow or frost.

207 –9997: a record of snow temperature sensor depth when the sensor was suspected to be located above,
208 not below the snow surface.

209 –8888: a record flagged during the manual masking procedure.

210 **4.1. Initial QC for Level 1.2 datasets**

211 The objectives of the initial control are to eliminate erroneous records due to mechanical
212 malfunctions or local phenomena and pre-treat Level 1.1 datasets for the secondary control. The initial
213 control consists of a range test (e.g., Fiebrich et al., 2010; Estévez et al., 2011) and a manual mask
214 procedure. The range test sets variation ranges (see Tables 3 and 4) for each observed parameter in
215 northwest Greenland on the basis of simple statistics based on maximum, minimum, and mean values
216 derived from records in the Level 1.1 dataset during a period with no obvious erroneous data. Records
217 outside this statistical range are flagged with a “–9999” code. Tables 3 and 4 list the parameters
218 subjected to this test and their assigned ranges. The manual masking procedure identified specific
219 erroneous values that resulted from an electrical malfunction and flagged them with a “–8888” code.
220 The following subsections offer detailed and additional explanations of the initial control, however,
221 the range test for each parameter is listed in Table 3, in the detail description of it for each parameter
222 is omitted in the following sections.

223 **4.1.1. Wind speed and wind direction**

224 U_{\max} used in the range test is the maximum value between the beginning of observation and 31
225 August 2020, and $+15.0 \text{ m s}^{-1}$ was taken as the range margin for the upper limit of U_n . In addition to
226 the range test, the following basic processing was also performed. When U_n was zero (no wind), WD_n
227 was flagged as erroneous:

$$228 \quad U_n = 0 \text{ and } WD_n > 0 \rightarrow WD_n \text{ flagged } -9999. \quad (1.1.1)$$

229 When WD_n had a negative value, it was flagged as erroneous:

$$230 \quad WD_n \leq 0 \rightarrow WD_n \text{ flagged } -9999. \quad (1.1.2)$$

231 **4.1.2. Air temperature and relative humidity**

232 $T_{n_{\max}}$ and $T_{n_{\min}}$ were determined from the entire observation period. The range margin for T_n was

233 set as ± 10.0 °C. Discrepancies arising from the dual sensors at SIGMA-A were addressed in the
 234 secondary control (see Sect. 4.2.2).

235 4.1.3. Shortwave and near-infrared radiation

236 The main objective of the initial control for shortwave radiation was to mask erroneous records
 237 attributed to Zero Offset (Behrens, 2021). Zero Offset is a few watts of radiation that occurs at night
 238 caused by the slight temperature difference between the two detectors (inside of the dome shelter and
 239 sensor body). However, since the value is an observation error, the observed value may be different
 240 from the original radiation balance and need to be masked.

241 The range test is based on the assumption that SW_d cannot exceed the maximum of SW_{TOA}
 242 (SW_{TOA_max}) during the observation period (761.6 W m^{-2} at SIGMA-A and 772.2 W m^{-2} at SIGMA-
 243 B), and albedos a_{sw} and a_{nir} cannot be higher than a_{sw_max} and a_{nir_max} ($a_{sw_max} = 0.95$ and $a_{nir_max} =$
 244 0.90), respectively, as determined from the radiative transfer model calculation (Aoki et al., 2003).
 245 Moreover, the fraction of the near-infrared spectral domain at the top of the atmosphere (f_{nir}) is
 246 assumed to be equal to 0.5151 based on the extraterrestrial spectral solar radiation (Wehrli, 1985).
 247 Based on those assumptions, upward and downward radiation fluxes were flagged as erroneous
 248 according to the range tests in Table 3.

249 The following procedures were also applied to mask erroneous records due to Zero Offset. These
 250 parameters were flagged as erroneous (−9999) in a following case (using SW_χ as an example):

$$251 \quad SW_\chi < 0 \text{ and } solz < 90.0 \rightarrow SW_\chi \text{ flagged } -9999, \quad (1.3.1)$$

$$252 \quad SW_\chi < 0 \text{ and } solz \geq 90.0 \rightarrow SW_\chi = 0. \quad (1.3.2)$$

253 4.1.4. Longwave radiation

254 The range tests were performed for LW_d and LW_u under the conditions in Table 3. LW_{d_max} and
 255 LW_{u_max} were determined as follows:

$$256 \quad LW_{d_max} = \varepsilon_{max} \sigma T_{max}, \quad (1.4.1)$$

$$257 \quad LW_{u_max} = \varepsilon \sigma T_{s_max}. \quad (1.4.2)$$

258 However, T_{max} is T_{2A_max} for the SIGMA-A site and T_{1B_max} for the SIGMA-B site. Maximum values
 259 were determined under the following assumptions: (1) T_{2A} and T_{1B} cannot be larger than T_{2A_max} and
 260 T_{1B_max} , respectively, (2) atmospheric emissivity is set to unity (ε_{max}), and (3) the value of LW_{u_max} is
 261 determined as the amount of radiation corresponding to longwave emission at T_{s_max} ($= 10$ °C), which
 262 includes errors due to longwave emissions from the poles of the AWS system and similar sources, and
 263 that the emissivity of the snow/ice surface (ε) is 0.98 (Armstrong and Brun, 2008).

264 Both upward and downward longwave fluxes were considered erroneous when the sensor appeared
 265 to be covered with snow or frost:

$$266 \quad |LW_d - LW_u| \leq 1.0 \rightarrow LW_d \text{ and } LW_u \text{ flagged } -9998. \quad (1.4.3)$$

267 **4.1.5. Surface height**

268 The range test for surface height (sh) was imposed separately for each period between
 269 maintenances to the SIGMA-A site, when the main mast extension was adjusted to prevent the sensors
 270 from being buried in snow. (A single range test sufficed for SIGMA-B.) For each test, the range was
 271 set so that sh varied from the median by ± 100 cm or ± 150 cm, a margin that was determined depending
 272 on the variation of the data records in each period. The objective of this range test (Procedure 1.5.1;
 273 Table 3) was to mask the most obvious outliers. In addition, corrections were made to the sh records
 274 after each of three maintenance visits to the AWS at SIGMA-A.

275 **4.1.6. Atmospheric pressure**

276 P_{a_ave} used in the range test is the average atmospheric pressure for the observation period at each
 277 AWS site (Table 3). The additional margin that defined the range was ± 100 hPa.

278 **4.1.7. Snow temperature**

279 The range test for snow temperature was conducted using following threshold values; T_{1_min} is
 280 the minimum air temperature for the site and the upper threshold, 0.2 °C, incorporates the sensor’s
 281 absolute error of 0.15 °C and the requirement that the snow temperature cannot be positive.

282
 283 Table 3. Range test coverage for each parameter used in the QC procedures. The variable subscripts
 284 “n” (1 or 2) and χ indicate the distinction of sensors height and the direction of radiation flux (upward
 285 or downward), respectively.

parameter	variable	unit	range test		procedure No.
			value	range	
wind speed	U_1, U_2	$m\ s^{-1}$	$0 <$	$U_n < U_{max} + 15.0$	1.1.3
wind direction ^a	WD_1, WD_2	degree	$0 <$	$WD_n \leq 360$	1.1.4
air temperature	T_1, T_2	°C	$T_{n,min} - 10.0 <$	$T_n < T_{n,max} + 10.0$	1.2.1
relative humidity	RH_1, RH_2	%	$0 \equiv$	$RH_n \leq 100$	1.2.2
shortwave radiation	SW_d, SW_u	$W\ m^{-2}$	$SW_d < SW_{TOA,max}$		1.3.3
			$SW_u < SW_{TOA,max} \times a_{sw,min}$		1.3.5
near-infrared radiation ^b	NIR_d, NIR_u	$W\ m^{-2}$	$SW_d < T_{IA}\ (or\ B) \times SW_{TOA,max}$		2.3.2
			$NIR_d < f_{nir} \times SW_{TOA,max}$		1.3.4
			$NIR_u < f_{nir} \times SW_{TOA,max} \times a_{nir,max}$		1.3.6
surface albedo	a_{sw}	-	$NIR_d < T_{IA} \times f_{nir} \times SW_{TOA,max}$		2.3.3
			$0.6 < a_{sw} < 0.95$ (for October–April in SIGMA-A)		2.4.1
			$0.4 < a_{sw} < 0.95$ (for May–September in SIGMA-A)		2.4.2
			$0.4 < a_{sw} < 0.95$ (for October–April in SIGMA-B)		2.4.3
surface near-infrared albedo	a_{nir}	-	$0.1 < a_{sw} < 0.95$ (for May–September in SIGMA-B)		2.4.4
			$0.5 < a_{nir} < 0.90$ (for October–April in SIGMA-A)		2.4.5
longwave radiation	LW_d, LW_u	$W\ m^{-2}$	$0.3 < a_{nir} < 0.90$ (for May–September in SIGMA-A)		2.4.6
surface height	sh	cm	$0 <$	$LW_\chi < LW_{\chi,max}$	1.4.4
atmospheric pressure	P_a	hPa	$median_sh - 100.0$ or $150.0^c <$	$sh < median_sh + 100.0$ or 150.0^c	1.5.1
snow temperature ^b	st	°C	$P_{a,ave} - 100.0 <$	$P_a < P_{a,ave} + 100.0$	1.6.1
			$T_{1,min} - 10.0 <$	$st_n < 0.2$	1.7.1

^a in case of $U_n > 0$

^b only SIGMA-A site

^c the margin is changed depending on a variation of the data record in each applied period.

286

287

288 Table 4. Statistical values used in the range tests, determined from the entire observation period up to
 289 31 August 2020.

meteorological parameter	unit	threshold value			
		SIGMA-A		SIGMA-B	
		parameter name	value	parameter name	value
wind speed	m s^{-1}	U_{1A_max}	23.9	U_{1B_max}	21.9
		U_{2A_max}	25.5	–	–
air temperature	$^{\circ}\text{C}$	T_{1A_max}	7.2	T_{1B_max}	10.7
		T_{2A_max}	7.2	–	–
		T_{1A_min}	–49.9	T_{1B_min}	–40.5
		T_{2A_min}	–49.9	–	–
longwave radiation	W m^{-2}	LW_{dA_max}	418.8	LW_{dB_max}	440.1
		LW_{uA_max}	357.2	LW_{uB_max}	357.2
atmospheric pressure	hPa	P_{a_aveA}	833.1	P_{a_aveB}	894.2

290

291

292 4.2. Secondary QC for Level 1.3 datasets

293 The secondary control applies another range test, an anomaly test, and a manual mask procedure.
 294 The range test sets a more precise variation range than the initial control and masks erroneous data
 295 records. The anomaly test sets a median and standard deviation (SD), which govern statistical tests as
 296 follows;

$$297 \quad \beta < \text{median}_\beta + \text{SD}_\beta \times \gamma, \quad (2.0.1)$$

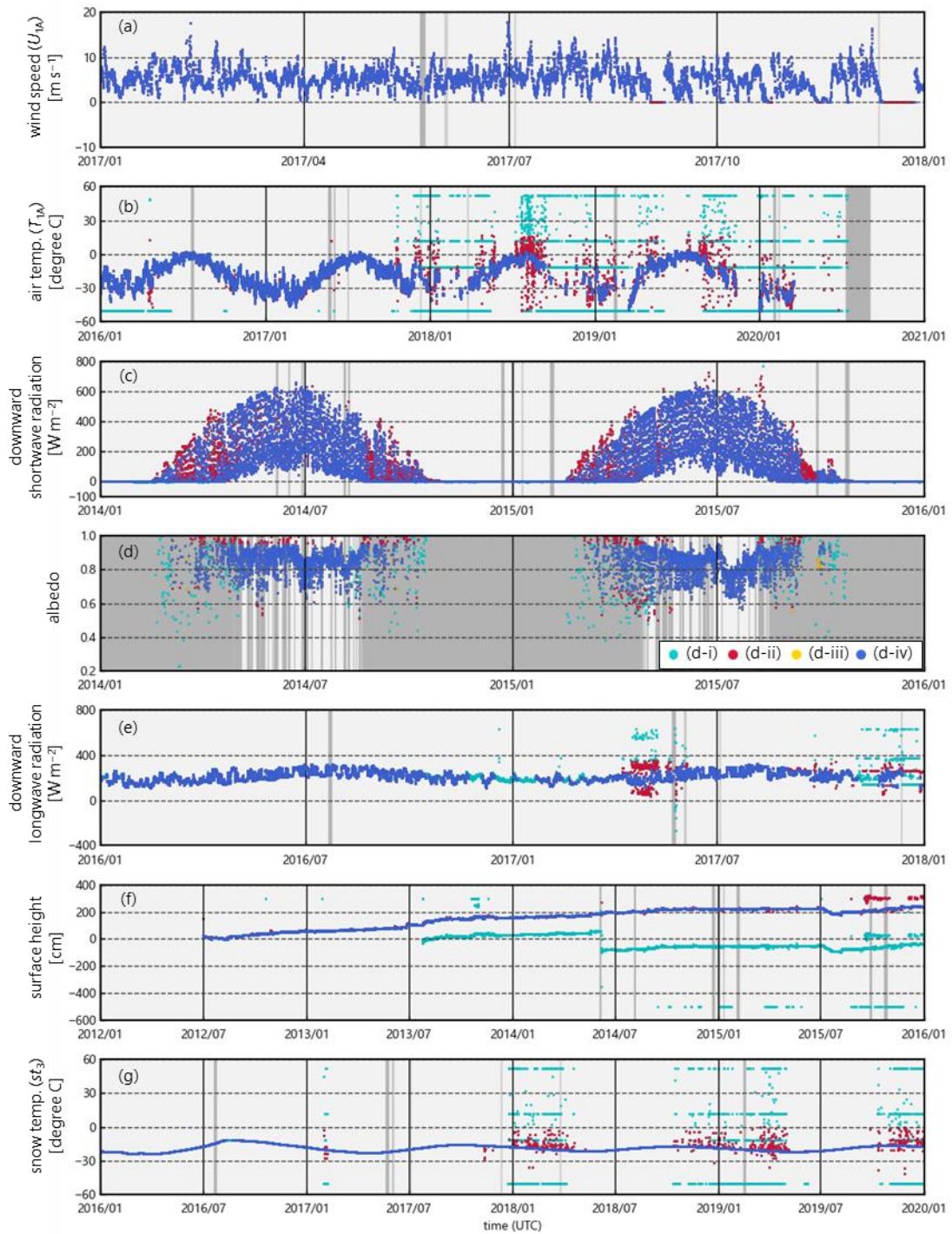
298 where β is an arbitrary variable and the multiplier γ is 1, 2, or 3 depending on the intensity of the
 299 anomaly variation, and determined based on the test results in each case. Those statistical values and
 300 the multiplier can be referred in the QC program. This study determined the possible range of correct
 301 values in the Level 1.2 dataset and identify and mask outliers if the variable deviates from its normal
 302 range. The manual mask procedure identifies and masks any remaining erroneous records. As a result
 303 of data masking by the initial control and the secondary control, the percentage of unmasked records
 304 for each parameter at three data levels is shown in Table 5, and the effects of the two controls are
 305 illustrated in Fig. 3 and described in detail below.

306

307 Table 5. Percentage of unmasked data for each parameter in each dataset.

308

	SIGMA-A			SIGMA-B		
	Level 1.1	Level 1.2	Level 1.3	Level 1.1	Level 1.2	Level 1.3
	%	%	%	%	%	%
U_1	98.0	98.0	92.1	99.7	99.7	97.7
WD_1	98.0	96.7	91.8	99.7	99.2	97.2
T_1	98.0	73.4	68.4	99.7	99.7	99.7
RH_1	98.0	50.7	43.6	99.7	99.7	98.8
U_2	98.0	98.0	94.1	–	–	–
WD_2	98.0	97.1	93.8	–	–	–
T_2	98.0	98.0	97.8	–	–	–
RH_2	98.0	98.0	98.0	–	–	–
SW_d	98.0	97.9	86.0	99.7	99.5	85.2
SW_u	98.0	97.9	97.8	99.7	99.7	99.7
LW_d	98.0	75.3	68.9	99.7	91.0	91.0
LW_u	98.0	68.7	67.4	99.7	91.0	91.0
NIR_d	98.0	97.9	86.4	–	–	–
NIR_u	98.0	97.9	97.8	–	–	–
sh	98.0	85.5	75.8	99.7	90.2	87.1
P_a	98.0	97.9	97.9	99.7	99.7	99.7
st_1	98.0	97.6	96.7	–	–	–
st_2	98.0	97.9	97.3	–	–	–
st_3	98.0	88.8	87.2	–	–	–
st_4	98.0	97.0	96.2	–	–	–
st_5	98.0	94.9	72.3	–	–	–
st_6	98.0	95.2	56.7	–	–	–
a_{sw}	–	–	31.6	–	–	32.4
a_{nir}	–	–	33.5	–	–	–
st_depth_1	–	–	75.8	–	–	–
st_depth_2	–	–	75.8	–	–	–
st_depth_3	–	–	75.8	–	–	–
st_depth_4	–	–	75.8	–	–	–
st_depth_5	–	–	52.7	–	–	–
st_depth_6	–	–	36.9	–	–	–
SW_{d_slope}	–	–	–	–	–	83.7



310

311 Figure 3. Examples of the initial and secondary controls for the SIGMA-A site: (a) wind speed (U_{1A}),
 312 (b) air temperature (T_{1A}), (c) downward shortwave radiation, (d) surface albedo, (e) downward
 313 longwave radiation, (f) surface height, and (g) snow temperature (st_3). In all panels except (d), the dark
 314 gray areas represent time periods in which data records in the Level 1.0 dataset were masked to
 315 produce the Level 1.1 dataset, light blue dots denote records masked by the initial control, red dots

316 denote records masked by the secondary control, and dark blue dots are the Level 1.3 data records. In
317 panel (d), the gray shaded area represents the masked (-9999) data records that cannot be calculated
318 due to the absence of, masked SW_d , or for other reasons. The light blue, red and yellow dots represent
319 data points masked by three QC operations during the secondary control; see Sect. 4.2.4 for
320 explanation.

321 4.2.1. Wind speed and wind direction

322 When U_n was zero for more than 6 continuous hours, U_n and WD_n were both flagged as erroneous
323 (-9999) under the assumption that the wind sensor was blocked by snow and ice. Although the initial
324 control eliminated no U_n records, this step masked many values in the winter (Fig. 3a).

325 4.2.2. Air temperature and relative humidity

326 Anomaly tests for air temperature and relative humidity were only applied to the lower-level sensor
327 records for SIGMA-A (i.e., T_{1A} and RH_{1A}). The anomaly test compared the difference (ΔT and ΔRH)
328 between readings of the upper and lower sensors (i.e., $|T_{1A} - T_{2A}|$ and $|RH_{1A} - RH_{2A}|$) to the
329 respective medians and SDs of those parameters. The medians were calculated from the data before 1
330 September 2017, because the data after that date appeared to include many erroneous T_{1A} records due
331 to deterioration of the data logger or sensor. The SD criterion (γ in Procedure 2.0.1) was adjusted
332 modestly ($\gamma = 3$) before 1 September, 2017 and more stringently ($\gamma = 1$) to detect outliers in the records
333 of T_{1A} and RH_{1A} after the date, which were flagged as erroneous (-9999). The effectiveness of this
334 adjustment is shown in Fig. 3b.

335 4.2.3. Shortwave and near-infrared radiation

336 The anomaly test for shortwave and near-infrared radiation was intended to mask the noise
337 resulting from a weak electric pulse at large solar zenith angles. The median and SD values were
338 calculated only from the records (SW_d , SW_u , NIR_d , and NIR_u) at $solz > 90.0^\circ$ to distinguish this noise
339 source according to Procedure 2.0.1 for above parameters, where $\gamma = 3$. If the record is in its anomaly
340 range, the records were identified as noise and modified to zero.

341 The downward radiation components were sometimes overestimated as a result of icing or riming
342 over the glass dome of the pyranometer. To mask these erroneous values, we applied range tests based
343 on SW_{TOA} and threshold values of atmospheric transmittance for each site T_{rA} and T_{rB} ($T_{rA} = 0.881$
344 and $T_{rB} = 0.872$) calculated by a radiative transfer model (Aoki et al., 1999, 2003) shown in Table 3.
345 Values of SW_d and NIR_d that were outside the range were flagged as erroneous (-9999).

346 To recognize other instances when the radiation sensor was covered with snow or frost, SW_d and
347 NIR_d records corresponding to the following case that downward radiation is smaller than upward

348 radiation was flagged as erroneous (−9998), using SW_{χ} as an example:

$$349 \quad SW_d < SW_u. \quad (2.3.1)$$

350 Figure 3c shows that the initial control eliminated a few erroneous SW_d data recorded in August 2015,
351 whereas the secondary control masked many records, especially in February–May, that were affected
352 by riming or frost.

353 4.2.4. Shortwave and near-infrared albedo

354 We calculated albedos a_{sw} and a_{nir} from the SW_d and NIR_d datasets that were passed the secondary
355 control. This calculation was done in four separate steps, shown by the color of dots in Fig. 3d.

356 (1) Flagging for low pyranometer sensitivity

357 At solar zenith angles near 90.0° , SW_d and NIR_d may not be an accurate measurement because of
358 the low sensitivity of the pyranometer. We therefore masked a_{sw} and a_{nir} values at $solz > 85.0^\circ$ or when
359 the SW_d (NIR_d) value was below the median SW_d (NIR_d) value for $solz > 85.0^\circ$. Records masked in this
360 step are shown in Fig. 3d as light blue dots (d-i).

361 (2) Range test for cold and warm periods

362 The range test used the upper and lower thresholds for a_{sw} and a_{nir} shown in Table 3, as determined
363 by the radiative transfer calculation of Aoki et al. (2003, 2011) plus a small error margin. Those
364 thresholds correspond to the assumed surface conditions during two parts of the year. For the cold
365 period of October–April, we used the lower thresholds for dry snow at the SIGMA-A site and dry or
366 wet snow at the SIGMA-B site conditions. For the warm period of May–September we used the
367 thresholds for wet snow at the SIGMA-A site and wet snow or dark ice at the SIGMA-B site conditions.
368 Records with albedo values beyond these theoretical thresholds were masked.

369 (3) Anomaly test in low atmospheric transmittance condition

370 The range test was augmented by an anomaly test to identify underestimates of a_{sw} and a_{nir} when
371 SW_d (NIR_d) was low and atmospheric transmittance (t_r) was small, typically at large solar zenith angles.
372 We masked a_{sw} (a_{nir}) values that were unnaturally low owing to low t_r and SW_d (NIR_d) in $solz > 80.0^\circ$
373 condition. Data records that were masked in either the range or anomaly tests are shown in Fig. 3d as
374 red dots (d-ii).

375 (4) Final steps

376 In cases where LW_d was flagged as “−9998” during the initial control (see Sect. 4.1.4), a_{sw} and a_{nir}
377 were flagged as “−9999” under the assumption that the radiation sensors were covered with snow or
378 frost. The final step was a manual mask procedure. Data records that were masked in this phase are
379 shown in Fig. 3d as orange dots (d-iii), and the final Level 1.3 dataset is displayed as blue dots (d-iv).

380 4.2.5. Longwave radiation

381 The anomaly test for LW_d and LW_u was conducted only for the SIGMA-A dataset using a standard

382 longwave radiant flux (LW_{std}), a measure of the amount of longwave radiation from the near-surface
 383 atmosphere that was calculated from the air temperature measurement by Brock and Arnold (2000)

$$384 \quad LW_{std} = \varepsilon^* \sigma (T_{2A} + 273.15)^4, \quad (\text{xi})$$

$$385 \quad \varepsilon^* = (1 + \kappa n) \varepsilon_0, \quad (\text{xii})$$

$$386 \quad \varepsilon_0 = 8.733 \times 10^{-3} \times (T_{2A} + 273.15)^{0.788}, \quad (\text{xiii})$$

387 where ε^* is the atmospheric emissivity, σ ($= 5.670 \times 10^{-8}$) is the Stefan–Boltzmann constant, κ ($=$
 388 0.26) is a constant depending on cloud type (Braithwaite and Olsen, 1990), n is the cloud cover
 389 amount (n : [0, 1] and set at 0.5 because it could not be determined), and ε_0 is the clear-sky emissivity.
 390 We assumed that LW_{std} was a close approximation of the true longwave radiant fluxes and used the
 391 absolute difference between LW_{std} and LW_d or LW_u (i.e., ΔLW_d or ΔLW_u) and its median and SD as the
 392 basis of the anomaly test as following Procedure 2.0.1.

393 Because parts of the LW_d dataset contained many erroneous records attributed to degradation of
 394 the data logger (see Fig. 3e), we reduced the SD criterion ($\gamma = 1$) in 7 April to 7 June 2017 and after 1
 395 September 2017. Except for those two periods, γ was set to “2” for both ΔLW_d and ΔLW_u . LW_d and
 396 LW_u records that were outliers under the criteria were flagged as erroneous (–9999). Figure 3e shows
 397 that the initial control (see Sect. 4.1.4) improved this anomaly test’s efficacy, and the secondary control
 398 yielded a clean LW_d time series.

399 4.2.6. Surface height

400 The anomaly test for surface height masked data that displayed unrealistic fluctuations.
 401 Differences (Δsh) were determined with respect to mean and SD values from the preceding 72 h values
 402 during period 1, before 1 September 2017 (sh_{mean1}) and period 2, after 1 September 2017 (sh_{mean2}). The
 403 Δsh values were compared to the median plus SD of Δsh for that period. In the period 1, the SD
 404 criterion in Procedure 2.0.1 was strict ($\gamma = 1$), and in the period 2, the criterion was relaxed ($\gamma = 3$). In
 405 addition, because surface height increased steadily in period 2, we derived the regression equation for
 406 this increase and identified outliers with respect to the SD of the regression, i.e. Δsh_{reg} as follows:

$$407 \quad \Delta sh_{reg} < SD_{reg_sh} \quad \text{for after 1 September 2017.} \quad (2.6.1)$$

408 Records of sh that varied beyond the anomaly ranges were flagged as erroneous (–9999).

409 A manual mask procedure was added as a final step. The result of QC procedure is shown in Fig.
 410 3f. The initial control, which corrected gaps resulting from the AWS maintenance (see Sect. 4.1.5),
 411 yielded the smoothed data record that enabled the application of the anomaly test. Sensor height dataset
 412 was made using initial sensor height (3 or 6 m) and the QC completed temporal surface height data.
 413 Therefore, QC for sensor height data has already been implemented through the QC for surface height
 414 data.

415 4.2.7. Snow temperature

416 In the first step, data records were masked when the snow temperature sensor was suspected to be
417 located above the snow surface:

$$418 \quad st_depth_n < -1.0 \rightarrow st_n \text{ flagged } -9999. \quad (2.7.1)$$

419 where st_depth_n [cm] was calculated using surface height data and the initial setting depth of sensor
420 “n” (see Sect. 3). The threshold of st_depth_n included a margin of 1.0 cm to reflect the accuracy of the
421 surface height sensor. The st_n was flagged as “-9997” if we could not judge whether the snow
422 temperature sensor was located below the snow surface.

423 The anomaly test for st_n consisted of two procedures. The first procedure relied on a temperature
424 gap (Δst_{d1}) between st_4 and data from each of the other five levels (st_{not4}) (i.e., $\Delta st_{d1} = |st_4 - st_{not4}|$),
425 because st_4 had very few erroneous data. The SD criterion (γ) for this anomaly test was changed for
426 each parameter depending on the variability of the data. The second procedure used the difference
427 (Δst_{d2}) between st_n and its mean value st_{n_mean} from the previous 72 h ($\Delta st_{d2} = |st_n - st_{n_mean}|$),
428 calculated using the same method as sh_{mean} (see Sect. 4.2.6). The SD criteria (γ) were all unity in this
429 test. In both procedures, the median and SD terms were calculated from records for the full time period.
430 Records detected as outliers were flagged as “-9999”. Figure 3g shows the results of all procedures,
431 using st_3 as an example.

432 4.2.8. Atmospheric pressure

433 The time series of P_a included only a few erroneous records. We masked outliers on the basis of

$$434 \quad |P_a - P_{a_mean}| > 20.0, \quad (2.8.1)$$

435 where P_{a_mean} is the average for the past 3 h (excluding masked data records). We set the threshold at
436 20.0, a higher value than the SD, because using the SD could have masked valid records. This
437 threshold value of 20 hPa is set on the assumption that a 20 hPa pressure jump is unlikely to occur in
438 a few hours. This procedure success to mask properly only the erroneous data of both sites.

439 5. Temporal variations of meteorological parameters

440 This section shows the results of simple analyses of the Level 1.3 dataset.

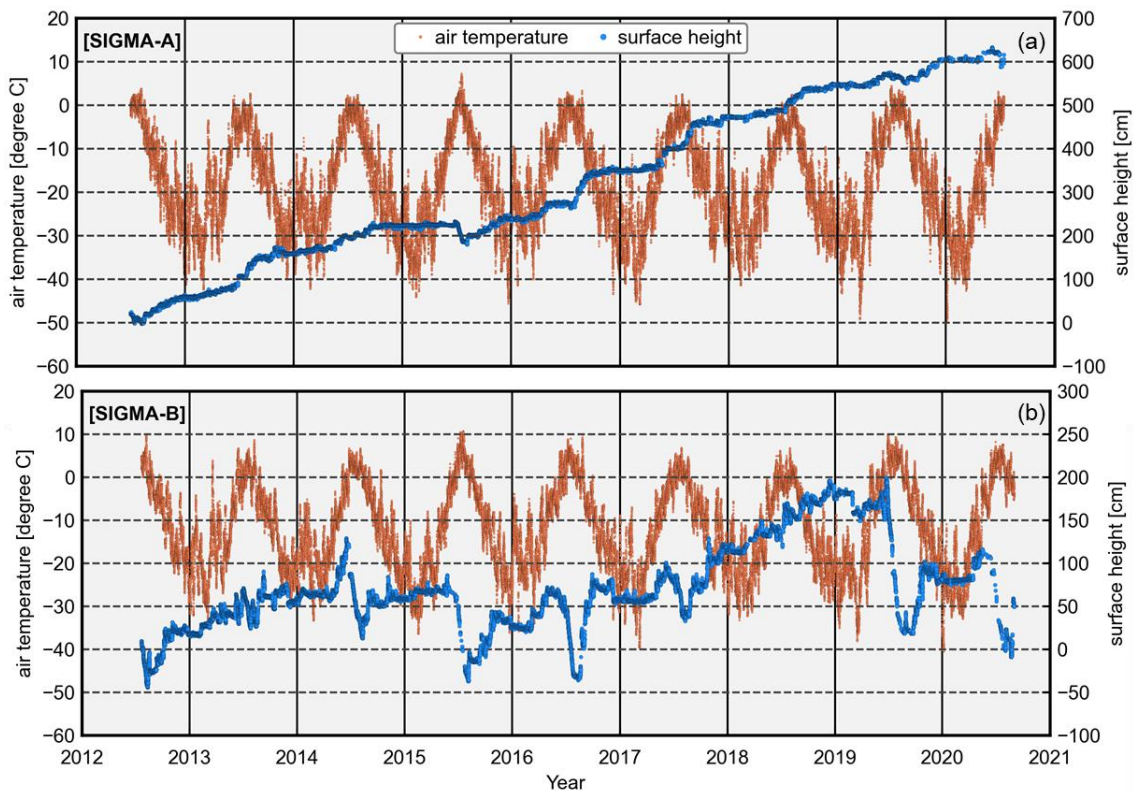
441 5.1. Air temperature and surface height

442 Figure 4 shows the air temperature fluctuations and surface height (sh) variations at both sites.
443 Mean air temperatures (2013–2019) were -18.1 °C at the SIGMA-A site and -12.3 °C at the SIGMA-
444 B site. The annual maxima of monthly data were recorded every July at both sites, except for August
445 2019 at the SIGMA-B site. At the SIGMA-A site, that annual maximum in 2015 was slightly positive

446 (+0.1 °C in July) but others were negative. At the SIGMA-B site, those were above freezing in all
 447 years. The annual minima occurred in different months between December and March. Unusually high
 448 hourly temperatures were recorded in mid-July 2015 (7.2 °C at SIGMA-A and 10.7 °C at SIGMA-B).
 449 Air temperatures exceeding 5.0 °C at SIGMA-A and 10.0 °C at SIGMA-B were common during that
 450 period.

451 Surface height steadily increased at the SIGMA-A site during the 8-year study period (Fig. 4), in
 452 which *sh* rose approximately 1 m in the mass-balance years (September to August) of 2013/14,
 453 2016/17, and 2017/18, and decreased slightly in the summers of 2011/12, 2014/15, and 2019/20.
 454 Accumulations were notable in autumn and relatively small in winter. At the SIGMA-B site, in contrast,
 455 increases and decreases in *sh* were observed during each mass-balance year. Decreases in *sh* during
 456 summers were rare during the summers of 2012/13 and 2017/18 but common during the 2013/14,
 457 2014/15, 2015/16, 2018/19, and 2019/20 summers, when decreases were greater than 1 m.

458



459

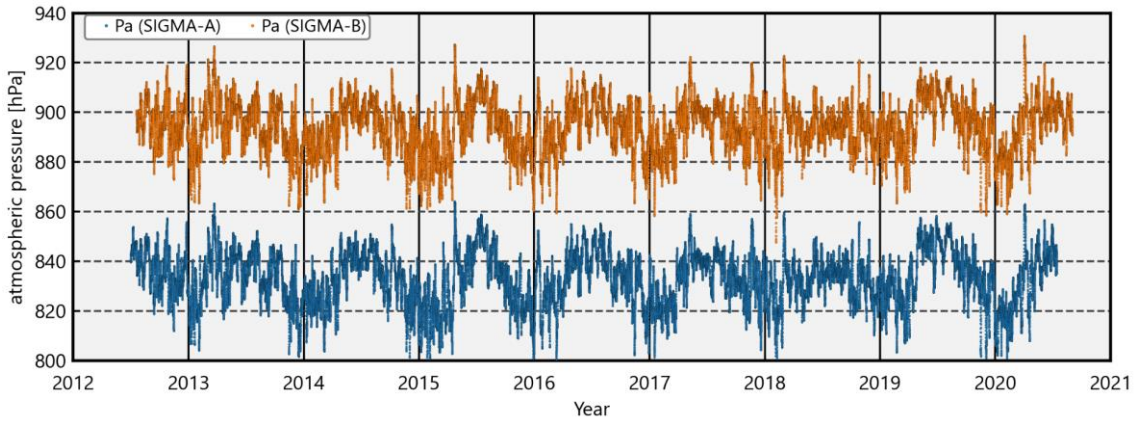
460 Figure 4. Time series of hourly air temperature and surface height at the (a) SIGMA-A (showing T_2
 461 data) and (b) SIGMA-B sites.

462

463 5.2. Atmospheric pressure and seasonal variation of temperature lapse rate

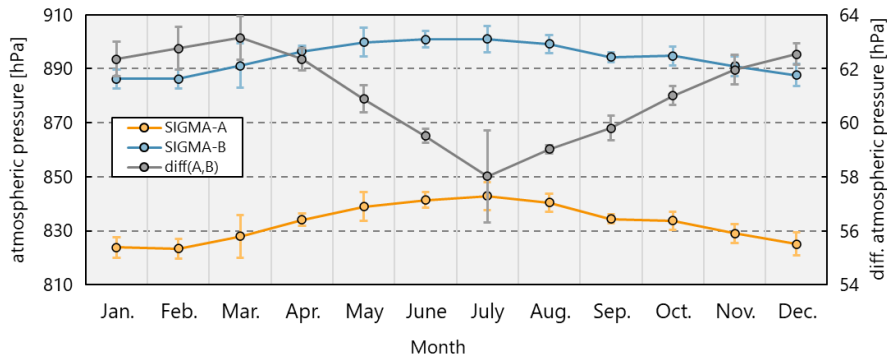
464 The time series of atmospheric pressure (P_a) at the SIGMA-A and SIGMA-B sites show a clear

465 seasonal variation, high in summer and low in winter (Fig. 6). The two data records had similar
 466 variation patterns that were strongly correlated ($r = 0.98$). The mean values for the whole observation
 467 period were 833.1 hPa at site SIGMA-A and 894.2 hPa at site SIGMA-B (Table 4). The difference in
 468 monthly mean P_a between the sites was smaller in summer and larger in winter (Fig. 7a), and the
 469 amplitude of the annual cycle was greater at the SIGMA-A site.
 470



471
 472 Figure 6. Time series of hourly atmospheric pressure (P_a) at the SIGMA-A and SIGMA-B sites.
 473

474

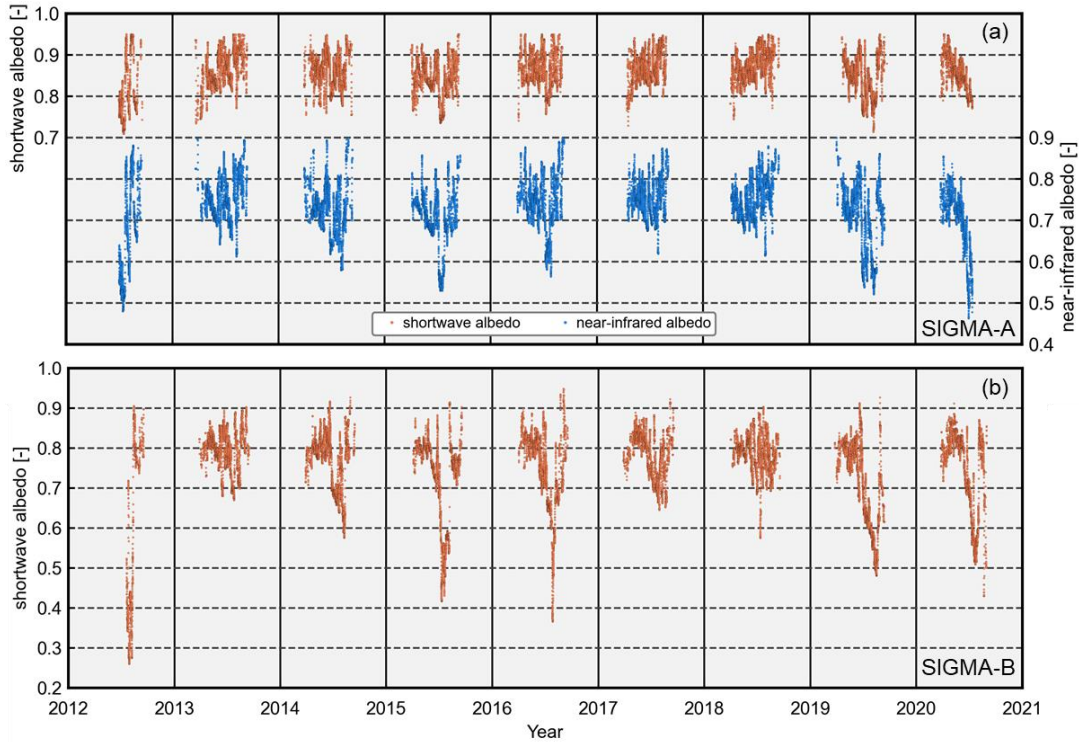


475
 476 Figure 7. Time series of ensemble averages of monthly mean atmospheric pressures during all years
 477 at both sites and their difference. Error bars indicate ± 1 SD.
 478

479 **5.3. Albedo**

480 Whereas shortwave albedo (a_{sw}) was rarely lower than 0.7 at site SIGMA-A, near-infrared albedo
 481 (a_{nir}) was below 0.6 in 2012, 2015, 2016, 2019, and 2020 (Fig. 8). Because a_{nir} depends on the snow
 482 grain size (Wiscombe and Warren, 1980), this finding implies that snow metamorphism progressed at
 483 the SIGMA-A site in those years (Hirose et al., 2021). A strong decrease in a_{sw} was observed at the
 484 SIGMA-B site during those same summers, which corresponded to notable decreases in surface height

485 (Fig. 4b) and high PDDs (Fig. 5). The decreases in albedo may have accelerated snowmelt and caused
 486 the decreases in surface height at SIGMA-B during the warm summers of those years (see Sect. 5.1).
 487 It appears that the difference in albedo reduction between the SIGMA-A and SIGMA-B sites in
 488 summer originated from the difference in air temperature between the sites.
 489
 490



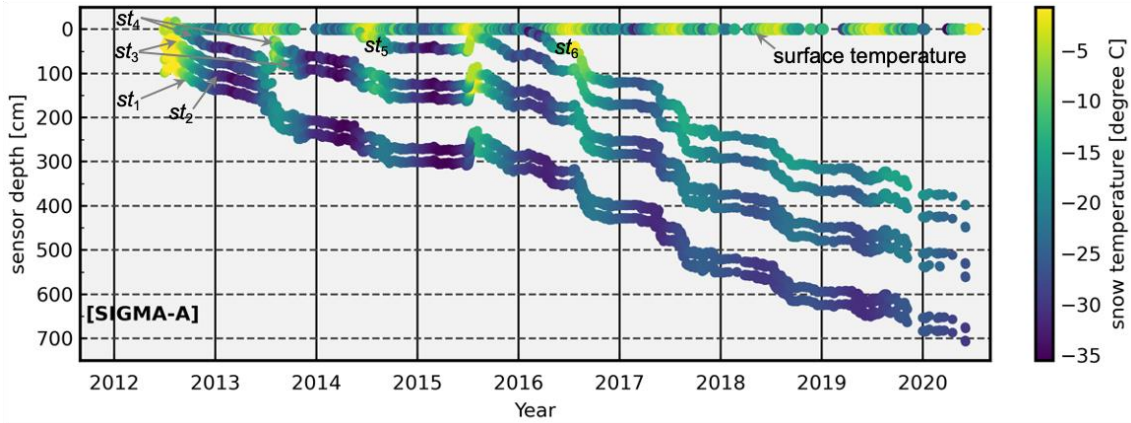
491
 492 Figure 8. Time series of hourly shortwave and near-infrared albedos at the (a) SIGMA-A and (b)
 493 SIGMA-B sites.
 494

495 **5.4. Snow temperature**

496 Figure 9 shows the time series of snow temperatures (st_1 – st_6) and snow sensor depths (st_depth_1 –
 497 st_depth_6). The sensor depths were calculated from each sensor’s initial depths (see Sect. 3.1) and the surface
 498 height variations at the SIGMA-A site. Seasonal and short-term snow temperature fluctuations were
 499 observed, which became smaller after the 2016/17 winter season, when snow accumulation was very
 500 large (Fig. 4). We assumed that the sensors were buried more deeply at that time, resulting in smaller
 501 fluctuations in snow temperature. The annual mean snow temperatures after 2016, a year in which
 502 snow temperatures were relatively stable and less variable, were between -18.9 ± 0.5 °C (st_4) and
 503 -19.5 ± 1.7 °C (st_5).

504 Sensors recorded relatively high snow temperatures when they were positioned at shallow depths

505 below the snow surface. However, in the summer of 2015, sensors st_3 and st_4 registered 0 °C even
 506 though they were more than 1 m below the snow surface. Air temperatures above freezing, and a large
 507 decrease in surface height were observed in this period (Figs. 4 and 5); thus, it is plausible that
 508 snowmelt occurred from the surface to depths near 120 cm, where st_3 was located at that time.
 509



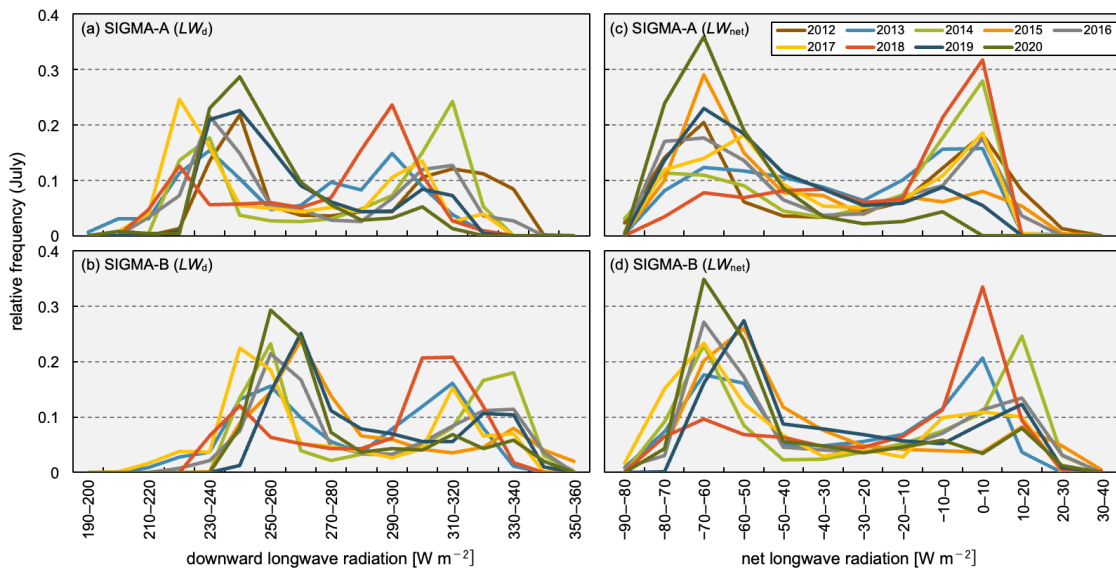
510
 511 Figure 9. Time series of hourly snow temperatures (st_1 – st_6), sensor depth, and surface temperature
 512 (calculated from upward longwave radiation) at the SIGMA-A site.
 513

514 5.5. Longwave radiation

515 The frequency distribution of longwave radiation, taken to represent the atmospheric condition, is
 516 often used as an indicator of climatological cloudiness (Stramler et al., 2011). Figure 10 shows the
 517 histograms of occurrence frequency of downward (LW_d) and net longwave radiation ($LW_{net} = LW_d -$
 518 LW_u) during July of all years at the SIGMA-A and SIGMA-B sites. The corresponding histograms for
 519 the four seasons (autumn: SON, winter: DJF, spring: MAM, summer: JJA) are shown in Figs. S1 and
 520 S2. The July LW_d data from both sites had bimodal distributions, with a lower mode of 220–240 $W m^{-2}$
 521 m^{-2} at SIGMA-A and 240–260 $W m^{-2}$ at SIGMA-B, and a higher mode of 290–310 $W m^{-2}$ at SIGMA-
 522 A and 310–330 $W m^{-2}$ at SIGMA-B. The histograms of July and seasonal LW_{net} had similar but clearer
 523 bimodal distributions, with modes at approximately 0 $W m^{-2}$ and $-70 W m^{-2}$ (Figs. 10c-d and S2).

524 LW_{net} can be regarded as an indicator of cloudiness, because blackbody radiation from the cloud
 525 cover increase both downward and net longwave radiation. Stramler et al. (2011) and Morrison et al.
 526 (2012) have argued that surface net longwave radiative flux has two modes in occurrence frequency
 527 (at $-40 W m^{-2}$ and 0 $W m^{-2}$), which correspond to clear-sky and overcast (low-level mixed-phase
 528 clouds) conditions. In overcast conditions, because the cloud base and the surface are in thermal
 529 equilibrium, the vertical thermal gradient is small and the longwave radiation budget is balanced (LW_{net}
 530 $= 0 W m^{-2}$) at the surface. The two modes of LW_{net} (0 $W m^{-2}$ and $-70 W m^{-2}$) at the two AWS sites
 531 appear to correspond to the modes proposed by these earlier studies.

532 The occurrence frequency of LW_{net} in JJA appears to be more variable than those for the other
533 seasons at both sites (Fig. S2). In these months, the air temperature rises and sea ice extent decreases,
534 increasing the water vapor supply and advection from the surrounding sea to coastal Greenland (Kim
535 and Kim, 2017; Liang et al., 2022). In such atmospheric conditions, the cloud formation process is
536 susceptible to synoptic-scale disturbances. The histogram of LW_{net} for July (Fig. 10) indicates a higher
537 frequency of clear-sky ($LW_{\text{net}} \cong -70 \text{ W m}^{-2}$) in 2015, 2019, and 2020 and overcast conditions (LW_{net}
538 $\cong 0 \text{ W m}^{-2}$) in 2014 and 2018. In SON and MAM, weather condition was less variable, and overcast
539 and clear-sky conditions dominated, respectively. Our analysis shows that cloudiness in JJA was more
540 variable than in other seasons, a result that is also borne out by satellite observations (Ryan et al.,
541 2022).
542



543
544 Figure 10. Histograms of the occurrence frequency of hourly downward longwave radiation (LW_d) and
545 net longwave radiation (LW_{net}) observed at the SIGMA-A and SIGMA-B sites in July of all years in
546 the study period. Each relative frequency represents the fraction of the total contained in each 10 W
547 m^{-2} bin.

548 6. Data availability

549 The Level 1.1, 1.2, and 1.3 datasets from this study are archived and available from the Arctic Data
550 archive System (ADS) in the National Institute of Polar Research (Table 6), where they are stored in
551 text (CSV) file format. Detailed information on the data content is presented in the file
552 “data_format_site-name_data-level.csv” associated with each of these dataset files.
553

554 Table 6. Information for the archived datasets from the SIGMA-A and SIGMA-B sites.

<i>SIGMA-A</i>	
Level 1.1	
data name:	Quality-controlled datasets of Automatic Weather Station (AWS) at SIGMA-A site from 2012 to 2020: Level: 1.1
file name:	SIGMA_AWS_SiteA_2012-2020_Lv1_1.csv
citation:	http://doi.org/10.17592/001.2022041301
reference:	Nishimura et al. (2023a)
Level 1.2	
data name:	Quality-controlled datasets of Automatic Weather Station (AWS) at SIGMA-A site from 2012 to 2020: Level: 1.2
file name:	SIGMA_AWS_SiteA_2012-2020_Lv1_2.csv
citation:	http://doi.org/10.17592/001.2022041302
reference:	Nishimura et al. (2023b)
Level 1.3	
data name:	Quality-controlled datasets of Automatic Weather Station (AWS) at SIGMA-A site from 2012 to 2020: Level: 1.3
file name:	SIGMA_AWS_SiteA_2012-2020_Lv1_3.csv
citation:	http://doi.org/10.17592/001.2022041303
reference:	Nishimura et al. (2023c)
<i>SIGMA-B</i>	
Level 1.1	
data name:	Quality-controlled datasets of Automatic Weather Station (AWS) at SIGMA-B site from 2012 to 2020: Level 1.1
file name:	SIGMA_AWS_SiteB_2012-2020_Lv1_1.csv
citation:	http://doi.org/10.17592/001.2022041304
reference:	Nishimura et al. (2023d)
Level 1.2	
data name:	Quality-controlled datasets of Automatic Weather Station (AWS) at SIGMA-B site from 2012 to 2020: Level 1.2
file name:	SIGMA_AWS_SiteB_2012-2020_Lv1_2.csv
citation:	http://doi.org/10.17592/001.2022041305
reference:	Nishimura et al. (2023e)
Level 1.3	
data name:	Quality-controlled datasets of Automatic Weather Station (AWS) at SIGMA-B site from 2012 to 2020: Level 1.3
file name:	SIGMA_AWS_SiteB_2012-2020_Lv1_3.csv
citation:	http://doi.org/10.17592/001.2022041306
reference:	Nishimura et al. (2023f)

555

556 7. Summary and conclusion

557 This paper describes the in situ meteorological datasets from the SIGMA-A and SIGMA-B AWS
 558 sites in northwest Greenland and details the QC methods used in preparing the datasets. At this time
 559 when drastic environmental change is proceeding in the Arctic region, sound meteorological data and
 560 QC methods are of ever-growing importance.

561 The QC method offered here consists of two basic steps. The first step, the initial control, masks
 562 observations that are affected by mechanical malfunctions or local phenomena and is a pre-treatment
 563 for the second QC step. This step uses simple statistics to set the range of permissible variation in
 564 northwest Greenland for each observational parameter and flags erroneous records on the basis of that
 565 variation range. The second QC step, the secondary control, masks erroneous observations based on

566 more stringent variation ranges as determined by the median and SD values of the full observation
567 record. The QC procedures offered here may be valuable for scientists developing their own QC efforts.

568 We presented examples of time series of air temperature, surface height, atmospheric pressure,
569 snow temperature, surface albedos, and longwave radiation based on the resulting hourly
570 meteorological dataset for 2012–2020 in northwest Greenland. We also extracted information on
571 climatological cloudiness based on LW_{net} data derived from these in situ ground observations. Our
572 primary findings are summarized in the following four points: (1) high air temperature in the 2015
573 summer and low surface albedos in 2016, 2019, and 2020 summers were recorded at both SIGMA-A
574 and SIGMA-B sites. (2) Apparent decreases in surface height occurred in 2015 at both AWS sites and
575 in 2016, 2019, and 2020 at the SIGMA-B site. (3) Observed atmospheric conditions in JJA were
576 relatively variable in northwest Greenland compared to the other seasons. (4) Frequent clear-sky
577 conditions typified the summers of 2015, 2019, and 2020.

578 The datasets described here are archived in the open access Arctic Data archive System for all
579 scientific communities. We anticipate that they will not only aid in understanding and monitoring the
580 current climate in northwest Greenland but also contribute more broadly to the advancement of polar
581 climate studies.

582

583 **Author contribution**

584 All authors, excluding M. Nishimura, established the AWS systems and supported their
585 maintenance. In addition, M. Nishimura developed and carried out the QC procedures and analyzed
586 the observation data, TA designed and led the study project and provided technical support for the QC
587 procedures, M. Niwano conducted pre-treatments for the meteorological data record and constructed
588 a fundamental algorithm of the QC procedures, TY supported the field observations, especially
589 logistical support, and KF provided advice on interpreting the observational data. All authors
590 participated in the interpretation of results and gave final approval for publication.

591 **Competing interests**

592 The authors declare that they have no conflict of interest.

593 **Acknowledgments**

594 We recognize all members of the SIGMA project, the GRENE-Arctic Project in Greenland, and
595 the Arctic Challenge for Sustainability II (ArCS II) project. We also thank all of those who supported
596 the field observations. In particular, we thank Y. Iizuka (Hokkaido University), Y. Kurosaki (Hokkaido
597 University), and A. Tsushima (Chiba University) for taking part in the field activities at the SIGMA-
598 A site and establishing the AWS and Y. Komuro (National Institute of Polar Research) for technical

599 advice. This study was conducted as a part of the “Snow Impurity and Glacial Microbe effects on
600 abrupt warming in the Arctic (SIGMA)” Project supported by the Japan Society for the Promotion of
601 Science Grant-in-Aid for Scientific Research numbers JP23221004 and JP16H01772, the Global
602 Change Observation Mission-Climate (GCOM-C) research project of the Japan Aerospace
603 Exploration Agency, and ArCS II Program Grant Number JPMXD1420318865. For the use of
604 NunaGIS (<http://en.nunagis.gl/>) operated by Asiaq, Greenland Survey, in preparing Fig. 1, we
605 acknowledge the National Snow and Ice Data Center’s QGreenland package (Moon et al., 2021). The
606 DEM data from Arctic DEMs were provided by the Polar Geospatial Center under NSF-OPP awards
607 1043681, 1559691, and 1542736. Finally, we are grateful to the two anonymous reviewers and to B.
608 Vandecrux and G. Wolfgang as reviewers, as well as to Topical Editor G. Tobias for their very helpful
609 comments on the manuscript. Their comments have greatly refined and enhanced the value of this
610 paper.

611 **References**

- 612 Aoki, T., Aoki, T., Fukabori, M., and Uchiyama, A.: Numerical simulation of the atmospheric effects
613 on snow albedo with a multiple scattering radiative transfer model for the atmosphere-snow system,
614 *J. Meteorol. Soc. Japan*, 77, 595-614, https://doi.org/10.2151/jmsj1965.77.2_595, 1999.
- 615 Aoki, T., Kuchiki, K., Niwano, M., Kodama, Y., Hosaka, M., and Tanaka, T.: Physically based snow
616 albedo model for calculating broadband albedos and the solar heating profile in snowpack for
617 general circulation models. *J. Geophys. Res.: Atmos.*, 116 (D11114), 1–22.
618 <https://doi.org/10.1029/2010JD015507>, 2011.
- 619 Aoki, T., Hachikubo, A., and Hori, M.: Effect of snow physical parameters on shortwave broadband
620 albedos, *J. Geophys. Res.*, 108, D19, 1–12. <https://doi.org/10.1029/2003jd003506>, 2003.
- 621 Aoki, T., Matoba, S., Uetake, J., Takeuchi, N., and Motoyama, H.: Field activities of the “Snow
622 Impurity and Glacial Microbe effects on abrupt warming in the Arctic” (SIGMA) Project in
623 Greenland in 2011-2013. *Bull. Glaciol. Res.*, 32, 3–20. <https://doi.org/10.5331/bgr.32.3>, 2014.
- 624 Armstrong, R. L. and Brun, E. (Eds.): Physical processes within the snow cover and their
625 parameterization, in *Snow and Climate: Physical Processes, Surface Energy Exchange and*
626 *Modeling*, Cambridge University Press, Cambridge N.Y., p. 58, 2008.
- 627 Behrens, K.: Radiation sensors, in: *Springer handbook of atmospheric measurements*, edited by: Foken,
628 T., Springer International Publishing, pp. 297–357, [https://doi.org/10.1007/978-3-030-52171-](https://doi.org/10.1007/978-3-030-52171-4_11)
629 [4_11](https://doi.org/10.1007/978-3-030-52171-4_11), 2021.
- 630 Braithwaite, R. J. and Olesen, O. B.: A simple energy-balance model to calculate ice ablation at the
631 margin of the Greenland ice sheet. *J. Glaciol.*, 36, 222–228.
632 <https://doi.org/10.1017/S0022143000009473>, 1990.

633 Brock, B. W. and Arnold, N. S.: A spreadsheet-based (Microsoft Excel) point surface energy balance
634 model for glacier and snow melt studies. *Earth Surf. Proc. Land.*, 25, 649–658.
635 [https://doi.org/10.1002/1096-9837\(200006\)25:6<649::AID-ESP97>3.0.CO;2-U](https://doi.org/10.1002/1096-9837(200006)25:6<649::AID-ESP97>3.0.CO;2-U), 2000.

636 Estévez, J., Gavilán, P., and Giráldez, J. V.: Guidelines on validation procedures for meteorological
637 data from automatic weather stations, *J. Hydrol.*, 402, 144–154.
638 <https://doi.org/10.1016/j.jhydrol.2011.02.031>, 2011.

639 Fausto, R. S., van As, D., Mankoff, K. D., Vandecrux, B., Citterio, M., Ahlstrøm, A. P., Andersen, S.
640 B., Colgan, W., Karlsson, N. B., Kjeldsen, K. K., Korsgaard, N. J., Larsen, S. H., Nielsen, S.,
641 Pedersen, A., Shields, C. L., Solgaard, A. M., and Box, J. E.: Programme for Monitoring of the
642 Greenland Ice Sheet (PROMICE) automatic weather station data. *Earth Syst. Sci. Data*, 13, 3819–
643 3845. <https://doi.org/10.5194/essd-13-3819-2021>, 2021.

644 Fiebrich, C. A., Morgan, Y. R., McCombs, A. G., Hall, P. K., and McPherson, R. A.: Quality assurance
645 procedures for mesoscale meteorological data. *J. Atmos. Ocean. Tech.*, 27, 1565–1582.
646 <https://doi.org/10.1175/2010JTECHA1433.1>, 2010.

647 Fröhlich, C.: Total solar irradiance observations. *Surv. Geophys*, 33, 453–473.
648 <https://doi.org/10.1007/s10712-011-9168-5>, 2012.

649 Fujita, K., Matoba, S., Iizuka, Y., Takeuchi, N., Tsushima, A., Kurosaki, Y., and Aoki, T.: Physically
650 based summer temperature reconstruction from melt layers in ice cores. *Earth Space Sci.*,
651 8(e2020EA001590), 1–17. <https://doi.org/10.1029/2020EA001590>, 2021.

652 Hirose, S., Aoki, T., Niwano, M., Matoba, S., Tanikawa T., Yamaguchi, S., , and Yamasaki, T.:
653 Surface energy balance observed at the SIGMA-A site on the northwest Greenland ice sheet (in
654 Japanese with English abstract). *Seppyo*, 83, 143–154, https://doi.org/10.5331/seppyo.83.2_143,
655 2021.

656 Hock, R. and Holmgren, B.: A distributed surface energy-balance model for complex topography and
657 its application to Storglaciären, Sweden, *J. Glaciol.*, 51, 25–36.
658 <https://doi.org/10.3189/172756505781829566>, 2005.

659 Jonsell, U., Hock, R., and Holmgren, B.: Spatial and temporal variations in albedo on Storglaciären,
660 Sweden, *J. Glaciol.*, 49, 59–68. <https://doi.org/10.3189/172756503781830980>, 2003.

661 Kim, H. M. and Kim, B. M.: Relative contributions of atmospheric energy transport and sea ice loss
662 to the recent warm arctic winter. *J. Clim.*, 30, 7441–7450. <https://doi.org/10.1175/JCLI-D-17-0157.1>, 2017.

664 Kurosaki, Y., Matoba, S., Iizuka, Y., Niwano, M., Tanikawa, T., Ando, T., Hori, A., Miyamoto, A.,
665 Fujita, S., and Aoki, T.: Reconstruction of sea ice concentration in northern Baffin Bay using
666 deuterium excess in a coastal ice core from the north-western Greenland Ice Sheet. *J. Geophys.*
667 *Res. Atmos.*, 125. <https://doi.org/10.1029/2019JD031668>, 2020.

668 Liang, Y., Bi, H., Huang, H., Lei, R., Liang, X., Cheng, B., and Wang, Y.: Contribution of warm and
669 moist atmospheric flow to a record minimum July sea ice extent of the Arctic in 2020. *The*
670 *Cryosphere*, 16, 1107–1123. <https://doi.org/10.5194/tc-16-1107-2022>, 2022.

671 Makkonen, L. and Laakso, T.: Humidity measurements in cold and humid environments. *Boundary-*
672 *Layer Meteorol.*, 116, 131–147. <https://doi.org/10.1007/s10546-004-7955-y>, 2005.

673 Matoba, S., Niwano, M., Tanikawa, T., Iizuka, Y., Yamasaki, T., Kurosaki, Y., Aoki, T., Hashimoto,
674 A., Hosaka, M., and Sugiyama, S.: Field activities at the SIGMA-A site, north-western Greenland
675 Ice Sheet, 2017. *Bull. Glaciol. Res.*, 36, 15–22. <https://doi.org/10.5331/BGR.18R01>, 2018.

676 Matoba, S., Yamaguchi, S., Tsushima, A., Aoki, T., and Sugiyama, S.: Surface mass balance variations
677 in a maritime area of the north-western Greenland Ice Sheet (in Japanese with English abstract).
678 *Low Temperature Science*, 75, 37–44, doi: 10.14943/lowtemsci.75.37, 2017.

679 Moon, T., Fisher, M., Harden, L., and Stafford, T.: QGreenland (v1.0.1) [software]. Available from
680 <https://qgreenland.org>. <https://doi.org/10.5281/zenodo.4558266>, 2021.

681 Moradi, I.: Quality control of global solar radiation using sunshine duration hours, *Energy*, 34, 1–6.
682 <https://doi.org/10.1016/j.energy.2008.09.006>, 2009.

683 Morino, S., Kurita, N., Hirasawa, N., Motoyama, H., Sugiura, K., Lazzara, M., Mikolajczyk, D.,
684 Welhouse, L., Keller, L., and Weidner, G.: Comparison of Ventilated and Unventilated Air
685 Temperature Measurements in Inland Dronning Maud Land on the East Antarctic Plateau. *J.*
686 *Atmos. and Ocean. Technol.*, 38, 2061–2070. <https://doi.org/10.1175/JTECH-D-21-0107.1>, 2021.

687 Morrison, H., De Boer, G., Feingold, G., Harrington, J., Shupe, M. D., and Sulia, K.: Resilience of
688 persistent Arctic mixed-phase clouds. *Nat. Geosci.*, 5, 11–17. <https://doi.org/10.1038/ngeo1332>,
689 2012.

690 Mougnot, J., Rignot, E., Bjørk, A. A., van den Broeke, M., Millan, R., Morlighem, M., Noël, B.,
691 Scheuchl, B., and Wood, M.: Forty-six years of Greenland Ice Sheet mass balance from 1972 to
692 2018, *P. Natl. Acad. Sci. USA*, 116, 9239–9244. <https://doi.org/10.1073/pnas.1904242116>, 2019.

693 Nishimura, M., T. Aoki, M. Niwano, S. Matoba, T. Tanikawa, S. Yamaguchi, T. Yamasaki, A.
694 Tsushima, K. Fujita, Y. Iizuka, Y. Kurosaki: Quality-controlled datasets of Automatic Weather
695 Station (AWS) at SIGMA-A site from 2012 to 2020: Level 1.1, 1.00, Arctic Data archive System
696 (ADS), Japan [dataset], <http://doi.org/10.17592/001.2022041301>, 2023a.

697 Nishimura, M., T. Aoki, M. Niwano, S. Matoba, T. Tanikawa, S. Yamaguchi, T. Yamasaki, A.
698 Tsushima, K. Fujita, Y. Iizuka, Y. Kurosaki: Quality-controlled datasets of Automatic Weather
699 Station (AWS) at SIGMA-A site from 2012 to 2020: Level 1.2, 1.20, Arctic Data archive System
700 (ADS), Japan [dataset], <http://doi.org/10.17592/001.2022041302>, 2023b.

701 Nishimura, M., T. Aoki, M. Niwano, S. Matoba, T. Tanikawa, S. Yamaguchi, T. Yamasaki, A.
702 Tsushima, K. Fujita, Y. Iizuka, Y. Kurosaki: Quality-controlled datasets of Automatic Weather

703 Station (AWS) at SIGMA-A site from 2012 to 2020: Level 1.3, 1.20, Arctic Data archive System
704 (ADS), Japan [dataset], <http://doi.org/10.17592/001.2022041303>, 2023c

705 Nishimura, M., T. Aoki, M. Niwano, S. Matoba, T. Tanikawa, S. Yamaguchi, T. Yamasaki, K. Fujita:
706 Quality-controlled datasets of Automatic Weather Station (AWS) at SIGMA-B site from 2012 to
707 2020: Level 1.1, 1.00, Arctic Data archive System (ADS), Japan [dataset],
708 <http://doi.org/10.17592/001.2022041304>, 2023d.

709 Nishimura, M., T. Aoki, M. Niwano, S. Matoba, T. Tanikawa, S. Yamaguchi, T. Yamasaki, K. Fujita:
710 Quality-controlled datasets of Automatic Weather Station (AWS) at SIGMA-B site from 2012 to
711 2020: Level 1.2, 1.10, Arctic Data archive System (ADS), Japan [dataset],
712 <http://doi.org/10.17592/001.2022041305>, 2023e.

713 Nishimura, M., T. Aoki, M. Niwano, S. Matoba, T. Tanikawa, S. Yamaguchi, T. Yamasaki, K. Fujita:
714 Quality-controlled datasets of Automatic Weather Station (AWS) at SIGMA-B site from 2012 to
715 2020: Level 1.3, 1.20, Arctic Data archive System (ADS), Japan [dataset],
716 <http://doi.org/10.17592/001.2022041306>, 2023f.

717 Niwano, M., Aoki, T., Matoba, S., Yamaguchi, S., Tanikawa, T., Kuchiki, K., and Motoyama, H.:
718 Numerical simulation of extreme snowmelt observed at the SIGMA-A site, northwest Greenland,
719 during summer 2012. *The Cryosphere*, 9, 971–988. <https://doi.org/10.5194/tc-9-971-2015>, 2015.

720 Niwano, M., Aoki, T., Hashimoto, A., Matoba, S., Yamaguchi, S., Tanikawa, T., Fujita, K., Tsushima,
721 A., Iizuka, Y., Shimada, R., and Hori, M.: NHM-SMAP: Spatially and temporally high-resolution
722 nonhydrostatic atmospheric model coupled with detailed snow process model for Greenland Ice
723 Sheet. *The Cryosphere*, 12, 635–655. <https://doi.org/10.5194/tc-12-635-2018>, 2018.

724 Niwano, M., Box, J. E., Wehrlé, A., Vandecrux, B., Colgan, W. T., and Cappelen, J.: Rainfall on the
725 Greenland Ice Sheet: Present-day climatology from a high-resolution non-hydrostatic polar
726 regional climate model. *Geophys. Res. Lett.*, 48(e2021GL092942), 1–11.
727 <https://doi.org/10.1029/2021GL092942>, 2021.

728 Noël, B., van de Berg, W. J., Lhermitte, S., and van den Broeke, M. R.: Rapid ablation zone expansion
729 amplifies north Greenland mass loss, *Sci. Adv.*, 5, 2–11. <https://doi.org/10.1126/sciadv.aaw0123>,
730 2019.

731 Onuma, Y., Takeuchi, N., Tanaka, S., Nagatsuka, N., Niwano, M., and Aoki, T.: Observations and
732 modelling of algal growth on a snowpack in north-western Greenland. *The Cryosphere*, 12, 2147–
733 2158. <https://doi.org/10.5194/tc-12-2147-2018>, 2018.

734 Porter, C., Morin, P., Howat, I., Noh, M. J., Bates, B., Peterman, K., Keeseey, S., Schlenk, M., Gardiner,
735 J., Tomko, K., Willis, M., Kelleher, C., Cloutier, M., Husby, E., Foga, S., Nakamura, H., Platson,
736 M., Wethington, M. Jr., Williamson, C., Bauer, G., Enos, J., Arnold, G., Kramer, W., Becker, P.,
737 Doshi, A., D’Souza, C., Cummins, P., Laurier, F., Bojesen, M.: “ArcticDEM”,

738 <https://doi.org/10.7910/DVN/OHHUKH>, Harvard Dataverse, V1, [Accessed in January 18, 2022],
739 2018.

740 Rottman, G.: Measurement of total and spectral solar irradiance. *Space Sci. Rev.*, 125, 39–51.
741 <https://doi.org/10.1007/s11214-006-9045-6>, 2006.

742 Ryan, J. C., Smith, L. C., Cooley, S. W., Pearson, B., Wever, N., Keenan, E., and Lenaerts, J. T. M.:
743 Decreasing surface albedo signifies a growing importance of clouds for Greenland Ice Sheet
744 meltwater production. *Nat. Comm.*, 13(4205), 1–8. <https://doi.org/10.1038/s41467-022-31434-w>,
745 2022.

746 Steffen, C. and Box, J. E.: Surface climatology of the Greenland ice sheet: Greenland Climate Network
747 1995-1999, *J. Geophys. Res.*, 106, D24, 33951–33964, 2001.

748 Stramler, K., Del Genio, A. D., and Rossow, W. B.: Synoptically driven Arctic winter states. *J. Clim.*,
749 24, 1747–1762. <https://doi.org/10.1175/2010JCLI3817.1>, 2011.

750 Sugiyama, S., Sakakibara, D., Matsuno, S., Yamaguchi, S., Matoba, S., and Aoki, T.: Initial field
751 observations on Qaanaaq ice cap, north-western Greenland, *Ann. Glaciol.*, 55, 25–33.
752 <https://doi.org/10.3189/2014AoG66A102>, 2014.

753 Takeuchi, N., Sakaki, R., Uetake, J., Nagatsuka, N., Shimada, R., Niwano, M., and Aoki, T.: Temporal
754 variations of cryoconite holes and cryoconite coverage on the ablation ice surface of Qaanaaq
755 Glacier in northwest Greenland. *Ann. Glaciol.*, 59, 21–30. <https://doi.org/10.1017/aog.2018.19>,
756 2018.

757 Tanikawa, T., Hori, M., Aoki, T., Hachikubo, A., Kuchiki, K., Niwano, M., Matoba, S., Yamaguchi, S.,
758 and Stamnes, K.: In situ measurements of polarization properties of snow surface under the
759 Brewster geometry in Hokkaido, Japan, and northwest Greenland ice sheet. *J. Geophys. Res.*, 119,
760 13,946-13,964. <https://doi.org/10.1002/2014JD022325>, 2014.

761 Tsutaki, S., Sugiyama, S., Sakakibara, D., Aoki, T., and Niwano, M.: Surface mass balance, ice
762 velocity and near-surface ice temperature on Qaanaaq Ice Cap, north-western Greenland, from
763 2012 to 2016, *Ann. Glaciol.*, 58, 181–192. <https://doi.org/10.1017/aog.2017.7>, 2017.

764 van As, D., Fausto, R. S., Ahlstrøm, A. P., Andersen, S. B., Andersen, M. L., Citterio, M., Edelvang,
765 K., Gravesen, P., Machguth, H., Nick, F. M., Nielsen, S., and Anker, W.: Programme for
766 Monitoring of the Greenland Ice Sheet (PROMICE): First temperature and ablation records, *Geol.*
767 *Surv. Den. Greenl.*, 23, 73–76. <https://doi.org/10.34194/geusb.v23.4876>, 2011.

768 van den Broeke, M., van As, D., Reijmer, C., and van de Wal, R.: Assessing and improving the quality
769 of unattended radiation observations in Antarctica, *J. Atmos. Ocean. Tech.*, 21, 1417–1431.
770 [https://doi.org/10.1175/1520-0426\(2004\)021<1417:AAITQO>2.0.CO;2](https://doi.org/10.1175/1520-0426(2004)021<1417:AAITQO>2.0.CO;2), 2004a.

771 van den Broeke, M., Reijmer, C., and van de Wal, R.: Surface radiation balance in Antarctica as
772 measured with automatic weather stations, *J. Geophys. Res.*, 109, D09103, 1–17.
773 <https://doi.org/10.1029/2003JD004394>, 2004b.

774 van de Wal, R. S. W., Greuell, W., Van den Broeke, M. R., Reijmer, C. J., and Oerlemans, J.: Surface
775 mass-balance observations and automatic weather station data along a transect near Kangerlussuaq,
776 West Greenland. *Ann. Glaciol.*, 42, 311–316. <https://doi.org/10.3189/172756405781812529>, 2005.
777 Wehrli, C.: World Radiation Center (WRC) Publication. Davos-Dorf, Switzerland, 615, pp. 10-17,
778 1985.
779 Wiscombe, W. J., and Warren S. G.: A model for the spectral albedo of snow. I, Pure snow. *J. Atmos.*
780 *Sci.*, 37, 2712–2733., 1980.
781 Yamaguchi, S., Matoba, S., Yamazaki, T., Tsushima, A., Niwano, M., Tanikawa, T., and Aoki, T.:
782 Glaciological observations in 2012 and 2013 at SIGMA-A site, Northwest Greenland. *Bull.*
783 *Glaciol. Res.*, 32, 95–105. <https://doi.org/10.5331/bgr.32.95>, 2014.